83rd Steelmaking Conference Proceedings, (Pittsburgh, PA, March 26-29, 2000), Vol. 83, Iron and Steel Society, Warrendale, PA, 2000. pp. 541-557.

Transient Flow Structures in Continuous Casting of Steel

Sivaraj Sivaramakrishnan[*] , Hua Bai[*],
Brian G. Thomas[*], S. Pratap Vanka[*], and
Pierre H. Dauby[†], Mohammad B. Assar[†]

*Dept. of Mechanical and Industrial Engineering
University of Illinois at Urbana Champaign
1206 West Green Street, Urbana IL 61801
Ph: 217-333-6919 Fax: 217-244-6534

[†]LTV Steel Technology Center
Independence, OH 44131
Ph: 216-642-7255; Fax: 216-642-4599

Key Words: steel, water model, transient fluid flow, MFC, sensor, numerical models, particle image velocimetry

ABSTRACT

Transient flow events can be very important to the generation of quality problems during the continuous casting of steel. In this work, several different tools are applied to investigate these phenomena. Transient flow is computed using Large Eddy Simulation (LES) models, while conventional K-ε models yield time-averaged results. Particle Image Velocimetry (PIV) is applied to measure quantitatively the transient velocity fields in a water model of the nozzle and mold region. Electromagnetic (MFC) sensors on the wideface of an actual slab caster are used to measure the liquid steel velocity at four locations. Results using all four methods compare favorably for single-phase flow and give new insight into the flow phenomena.

The slide gate creates a strong swirl at the outlet ports of the nozzle, which is also predicted using the K-ε model. This swirl is seen to persist more than halfway across the mold, causing a characteristic staircase velocity vector pattern in the PIV measurements when viewed in a plane parallel to the wide faces. Flow across the top surface was found in PIV to contain periods of 5-10s when the velocities were three to four times their mean values. This is likely related to inlet conditions and would likely exacerbate shear entrainment of the liquid flux at the top surface and level fluctuations. Simulations of the MFC output indicate that accurate flow prediction is not possible unless the sensors are located in a region of relatively uniform flow, such as near the top surface. In both LES and PIV, the upper roll structure evolves chaotically between a single large recirculation structure and a set of distinct vortices. The lower rolls in PIV are significantly asymmetric for very long periods of time (~ 1-hour) and go through a repeating sequence of features. One of these features involves a short circuit between the upward and downward flow in the lower roll, which is also seen in the simulation. This appears to be inherent to the turbulent nature of the flow and is likely important to inclusion particle and bubble entrapment.

INTRODUCTION

Flow in the mold region during the continuous casting of steel is of great interest because it influences many important phenomena, which have far-reaching consequences on strand quality. These include the flow and entrainment of the top surface powder / flux layers, top-surface contour and level fluctuations, and the entrapment of subsurface inclusions and gas bubbles.

Flow in the mold can be studied using mathematical models, physical water models, and plant measurements. The turbulent flow through the

nozzle and in the mold of the continuous caster has been studied extensively using computational models based on the Reynolds Averaged Navier Stokes (RANS) approach [1-3]. The most popular of these are steady models using the K-ε turbulence model. In this work, the detailed evolution of the flow structures is also studied using the Large Eddy Simulation (LES) approach. LES is computationally much more intensive than K-ε, but offers a new level of insight into transient phenomena.

Scale water models have been applied with great success in previous work to study the flow of molten steel, owing to the similar kinematic viscosity of the two fluids, which governs much of the flow behavior. To better visualize and quantify the flow in these water models, Particle Image Velocimetry (PIV) has been applied recently to measure the instantaneous velocity fields [4-6]. In this work, measurements are performed on a water model at the LTV Technology Center (Independence, OH) using a PIV system installed by DANTEC [7].

Finally, velocities in the molten steel flowing in the continuous casting mold can be measured indirectly from electromagnetic (MFC) sensors embedded in the mold walls. In this work, MFC sensors developed by AMEPA GmbH [8] were installed on the LTV Steel No. 1 slab caster in Cleveland to produce velocity histories at four locations [5].

In this paper, recent results using all four of these methods are compared and applied to yield new insights into transient flow phenomena in the continuous casting nozzle and mold. This work is part of an ongoing effort to develop mathematical models of the continuous casting process and to apply them to increase understanding and solve problems of practical interest.

WATER MODEL AND PIV SETUP

The flow from the tundish passes through a slide gate, which moves at right angles to the wide face to restrict the opening in the nozzle and thereby control the flow rate. The flow then enters the mold cavity through the downward-angled square ports of the bifurcated nozzle, shown in Figure 1. Flow exits the bottom of the water model through three pipes attached to circular outlets in the bottom plate. Figure 2 shows a sketch of the experimental mold model, which is nominally symmetric with respect to the centerline shown in the figure. Table I lists the main dimensions and casting conditions for the nozzle and mold models. The thickness of the water model tapers from top to bottom in order to simulate only the liquid portion of the steel caster.

Flow visualization and velocity measurements were made using 0.4-scale Plexiglas water models of the tundish, nozzle and mold of the caster at LTV Steel Technology Center. Sequences of instantaneous velocity measurements were obtained using the PIV system [5]. The positions of tracer particles are recorded digitally when two consecutive pulses of laser light illuminate a planar section through the water. Knowing the time interval between pulses (1.5×10^{-3}s) and the distances moved by the particles (from image processing), a complete instantaneous velocity field is obtained. This procedure is usually repeated every 0.2s and the results from at least 50 such exposures are averaged to obtain the time-averaged velocity field. In order to get good resolution in the PIV measurements, the domain was divided into four regions: the vicinity near the nozzle ports, the top region of the mold containing the jet and the upper roll, the middle region containing both the lower rolls and the bottom region containing part of the lower roll.

NUMERICAL MODELS

Two different numerical flow models were developed for this work at the University of Illinois. Each satisfies mass and momentum conservation in the computational domain by solving the continuity equation and the conservative form of the Navier Stokes equations for isothermal incompressible Newtonian fluids.

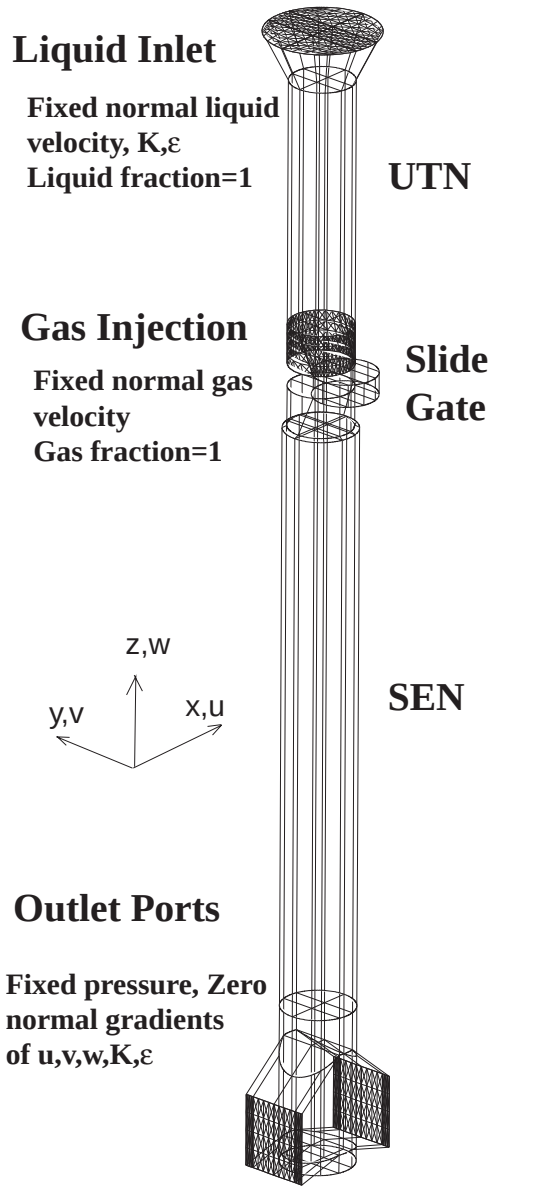

Fig. 1. Outline of slide gate nozzle and boundary conditions

$$\frac{\partial v_j}{\partial x_j} = 0 \qquad (1)$$

$$\frac{\partial}{\partial t}\rho v_i + \frac{\partial}{\partial x_j}\rho v_j v_i = -\frac{\partial P}{\partial x_i} + \frac{\partial}{\partial x_j}\mu_{eff}\left(\frac{\partial v_j}{\partial x_i} + \frac{\partial v_i}{\partial x_j}\right) \qquad (2\text{-}4)$$

The solution yields the pressure and velocity components at every point in the three-dimensional domain. At the high flow rates involved, these models must account for turbulence.

Table I – Water model conditions

Dimension / Condition	Value
Tundish bath depth	400~410 mm
Nozzle length (total)	510 mm
UTN diameter	28 mm
Slide-gate diameter	28 mm
Slide-gate thickness	18 mm
Slide-gate orientation	90°
Slide-gate opening (FL)	52%
SEN submergence depth (top of port to top surface)	77± 3 mm
Bore (SEN) diameter	32 mm
Port width x height	31mm x 32mm
Port thickness	11 mm
Port angle, lower edge	15^o down
Port angle, upper edge	40^o down
Bottom well recess depth	4.8 mm
Port opening	31 x 31 mm
Water model length	950 mm
Water model width (steel caster width)	735 mm (72 in. full scale)
Water model thickness (steel caster thickness)	95 mm (top) to 65 mm (bottom) (9. in. full scale)
Outlets at bottom of mold domain (both halves)	3 round 35mm diameter outlets
Casting speed (model top)	0.633 m/min
Liquid flow rate through each port	3.53×10^{-4} m^3/s (5.6gal/min)
Average velocity at port	424 mm/s
Average jet angle at port	30^o
Liquid kinematic viscosity	1.0×10^{-6} m^2/s
Gas injection	0%

Large Eddy Simulation (LES) Model

Large Eddy Simulation (LES) uses a fine grid to accurately capture details of the large-scale structures of the flow. For high velocities, a turbulence model is often used at the sub-grid scale in order to diffuse the kinetic energy of these scales, although this was not needed in the present work.

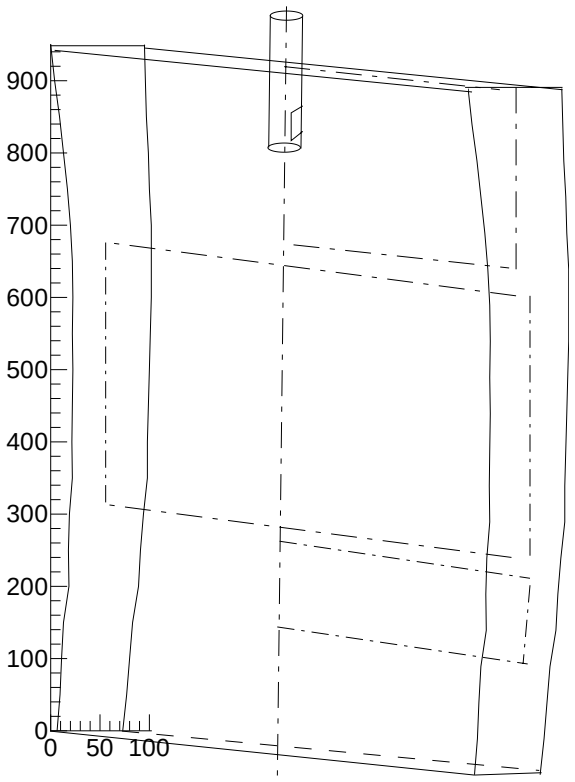

Fig. 2. Water model geometry

The equations in the LES model are discretized using the Harlow-Welch fractional step procedure [9] on a staggered grid. Second order central differencing is used for the convection terms and Crank Nicolson scheme [9] is used for the diffusion terms. The Adams-Bashforth scheme [9] is used to discretize in time with second order accuracy. The implicit diffusion terms are solved for using Alternate Line Inversion. The Pressure Poisson equation is solved using a direct Fast Fourier Transform solver. For parallelization, 1-D domain decomposition with MPI (Message Passing Interface) is used. A computational grid with 1.5 million nodes was used with a time step of 0.001s. The LES simulations are quite slow and take 18 CPU s per time step or 13 days (total CPU time) on an Origin 2000 for 60s of flow simulation. To simplify the computational domain, only the mold was simulated without the taper and rigid boundary for the free surface. The inlet was a fully-developed turbulent flow from a square duct at a downward angle of 30^o [10].

K-ε Model

For improved computational efficiency using a courser grid, the conventional K-ε model averages the effect of turbulence using an increased effective viscosity field. To model two-phase flow, an additional set of momentum conservation equations was solved for the argon gas phase. Interphase coupling terms were added to account for the drag in proportion to the relative velocities of the liquid and bubble phases, which were generally in the Stokes or Allen regimes. The equations were solved using the CFX v4.2 finite-difference package [11]. The nozzle domain used 10620 nodes and typically required 2.5 hours of computation. Further details are provided elsewhere [12].

NOZZLE RESULTS (SEN)

Flow Pattern Observations

Flow patterns observed in the experiments can be directly compared to the numerical simulation with the model described above under the same operation conditions. Simulations were conducted for the conditions in Table I, except that 5.8% gas was injected, and 1mm bubble diameter was assumed. The results were compared with PIV water model experiments using the same gas injection. In both the water experiments and model predictions, three main recirculation zones are observed inside the slide-gate nozzle: in the cavity of the middle gate plate, below the throttling gate plate, and at the nozzle ports. High gas concentration collects in these recirculation zones. Figure 3.1 shows an example of the predicted flow pattern looking into the left nozzle port. In both the simulation and the water experiments, the jet exits the ports with a single strong vortex or swirl. The vortex rotational direction is relatively stable with clockwise direction at the plane of the port exit. The jet is directed approximately 29° down, as seen in the photograph, Figure 3.2. This is very close to the value of 27.8° down calculated from the simulation results using a weighted-average method over all nodes on the port plane [13]. No obvious “back-

flow" at the nozzle port was observed during the experiments. It is noted that the observation of no back-flow differs from many previous findings for typical nozzles [2, 3].

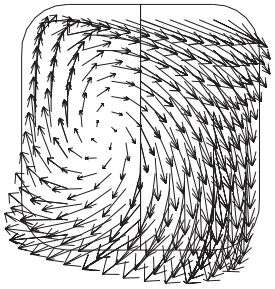

Fig. 3.1. Swirl pattern at nozzle port

The lack of any back-flow-zone in the experiments is mainly due to the special design of the SEN ports of this nozzle, which had a much steeper angle of the upper port edges (40° down) than the lower port edges (15° down).

Velocity Comparison (PIV and K-ε)

Quantitative comparisons between the PIV measurements and the K-ε simulation results were made on the jet at the nozzle port exit. An example is shown in Figure 4. Unfortunately, the flow field inside the plastic nozzle could not be reliably measured, due to the curvature of the nozzle wall and partial opacity from the machining cut. Figure 4 a) shows a vector plot of the PIV-measured flow field around the nozzle port in the plane parallel to the wide face of the mold. The predicted flow vector plots (b) are plotted side by side for direct visual comparison. The magnitudes of the liquid velocity at the port for measurements and prediction are then extracted and plotted together in (c). The "overall jet angle", defined as the weighted-average over the whole 3-D jet [3], should not be compared with the 2-D jet angle calculated from a single slice of the PIV measurements, or "slice jet angle". The slice jet angle is a simple arithmetic average of the jet angles for all measuring points (PIV) or computational cells (K-ε) at the slice of the nozzle port. The time-averaged values of the "slice jet angle" are marked on Figure 4 c).

The upper part of Figure 4 is for the slice through the nozzle center-plane (y=0), and the lower part for the slice that is away from and parallel to the center-plane (at y=12mm). The match of the velocity magnitude and the slice jet angle between the PIV measurement and the model prediction is satisfactory except that the velocity predictions are consistently slightly larger than the measurements. This is likely due to fact that the pulsed laser light sheet location was manually adjusted during the PIV experiments, and thus might not lie exactly in the desired position.

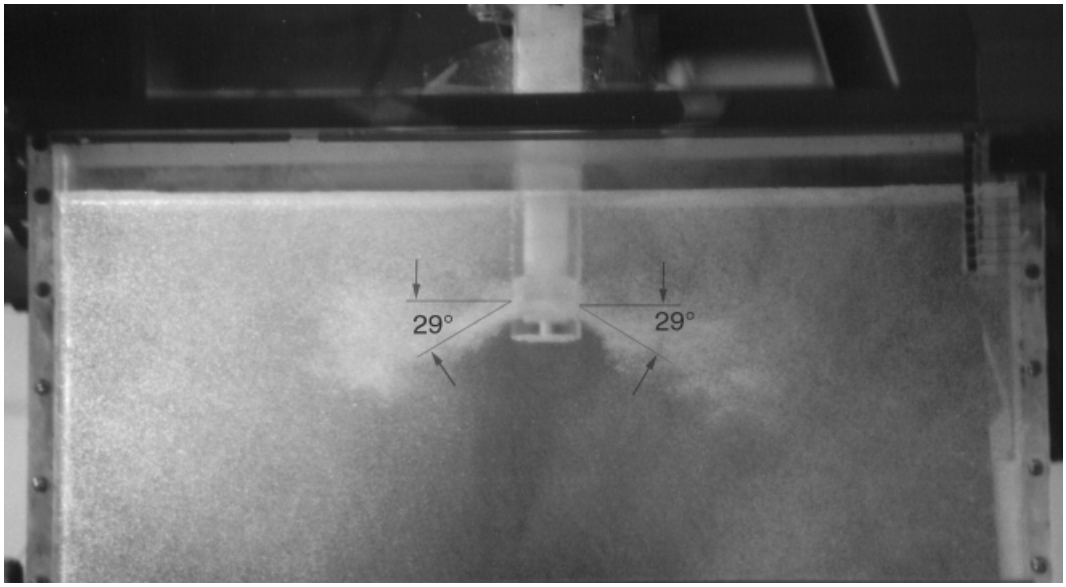

Fig. 3.2. Flow pattern and the average jet angle measurement in water model experiment

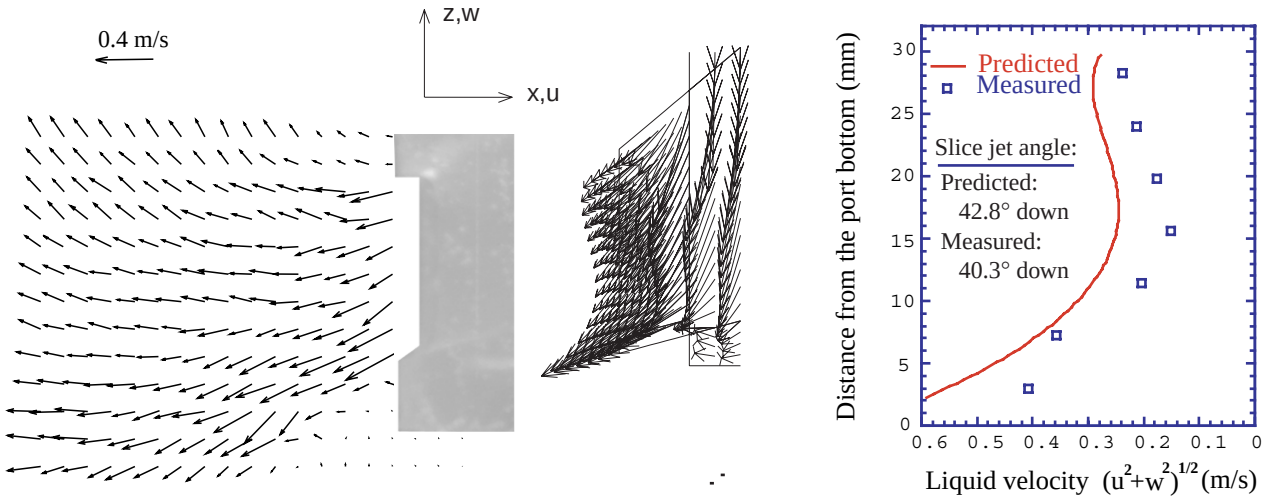

Slice (y=0) at the center-plane of the nozzle, parallel to the wide face of the mold

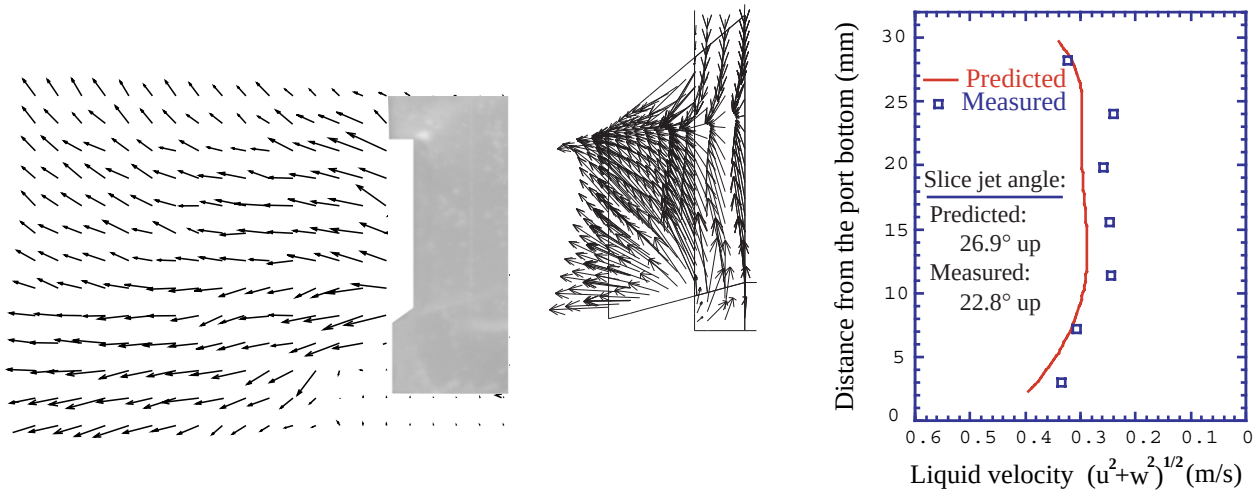

Slice (y=12mm) away from the center-plane of the nozzle, parallel to the wide face of the mold

(A) PIV measurements **(B) CFX prediction** **(C) Speed comparison**

Fig. 4. Comparison of PIV measurements and K-ε model predictions, showing downward flow from port centerline and upward flow at port edges due to swirl.

MOLD REGION RESULTS

Figure 5 shows a side to side comparison of a typical instantaneous vector plot along the center plane of the water model, parallel to the wide faces, obtained from the simulation (a) and PIV measurements (b) for the conditions in Table I.

Figure 6 compares the corresponding time averaged vector plots. The simulation vector plot is time averaged over 60s. The PIV vector plot is a composite containing three time-averaged parts. The three parts are the top region containing the upper roll and the jet which has been averaged over 10s (50 snapshots), the middle region containing the lower roll (0.25-0.65m below water surface) averaged over 200s (200 snapshots), and the bottom region extending from 0.65m - 0.77m averaged over 40s (200 snapshots). The middle region is also a spatial average of the right and left half regions of the water model, in order to average the considerable differences which arose due to asymmetry between sides.

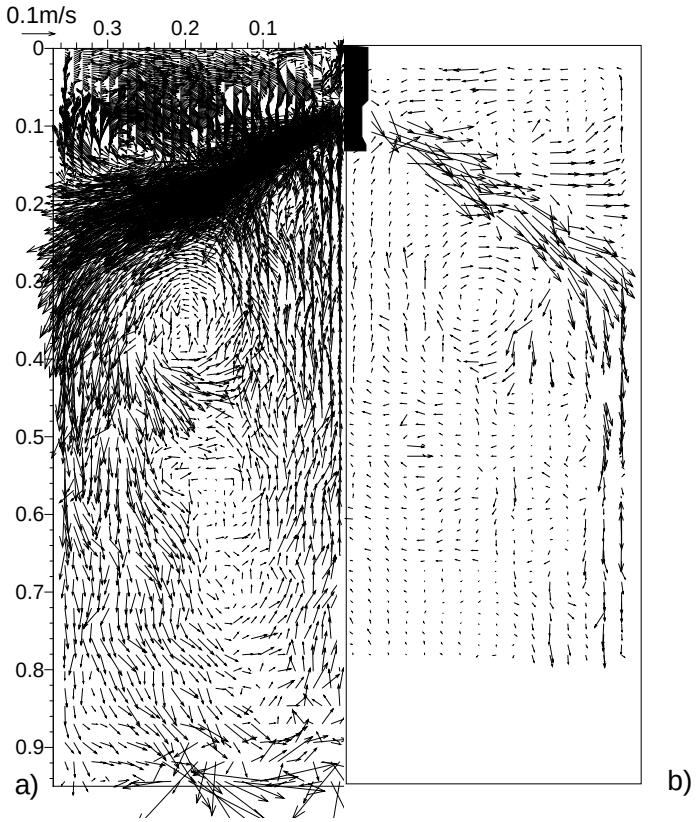

Fig. 5. Instantaneous velocity vector plot of (a) simulation and (b) PIV measurement

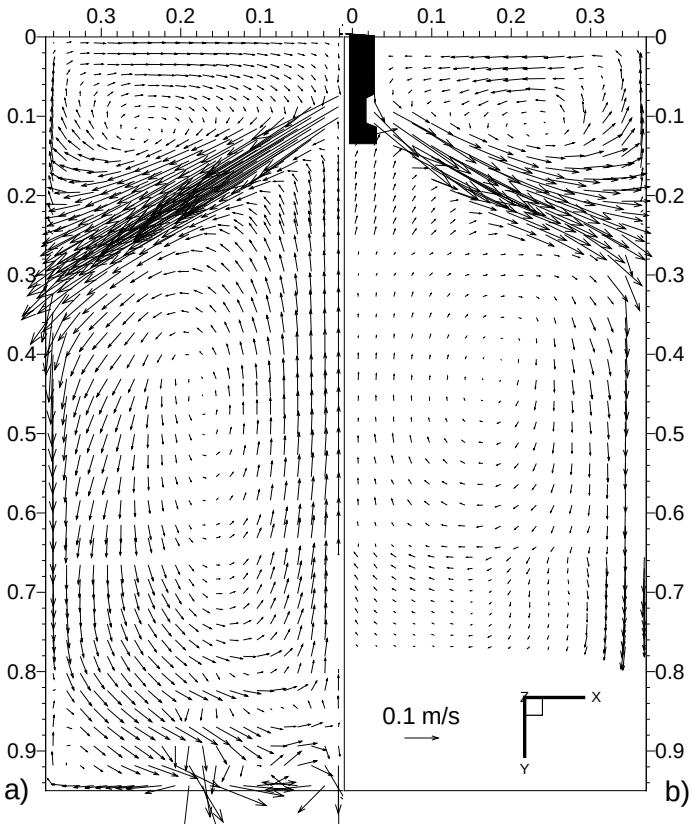

Fig. 6. Time averaged velocity vector plot of (a) simulation and (b) PIV measurement

The LES simulation and PIV experimental results generally match very well. Both the LES and PIV jets bend slightly upwards, as they traverse across the mold towards the narrow face. The biggest discrepancy is that the upward-moving velocities in the region directly below the SEN in the numerical simulation are larger than in the experiment.

LES and PIV in the Upper Mold

Figure 7 shows a sample plot of time variation of velocity at a typical point 20 mm below the top surface, halfway between the SEN and the narrow face. The PIV points are spaced 0.2s apart as compared to 0.001s increments in the simulation. The PIV velocity variation shows the existence of two time scales. The short time scale is about 0.7s and is predicted well by the simulation. The longer time scale is at least 45s. It results in times of 5s or more when the velocity close to the top surface is three to four times the mean. This period of high velocity could shear the molten flux layer and cause its entrainment deep into the caster. These long time-scale variations caused by the wide variations in the depth of penetration of the experimental jet are not seen in the simulation.

Figure 8 shows a schematic of the flow from the port that illustrates the swirling jet. The perpendicular movement of the slide gate flow control positioned high in the nozzle tube, (relative to the wide face) allows flow through only 41% of the nozzle bore area. This causes stronger flow down the inner-radius wide-face side of the nozzle. This bias in flow over the cross section continues causing the experimental jet to swirl as it exits the nozzle ports. This persists into the mold cavity, where the jet centerline moves along a helix, as depicted in the figure. The overall jet moves downward at an angle of 30^{o} and the swirl gradually diffuses. The swirling experimental jet moves both up-down and in-out of the center plane. As a result of the helical motion, strong regions of the flow

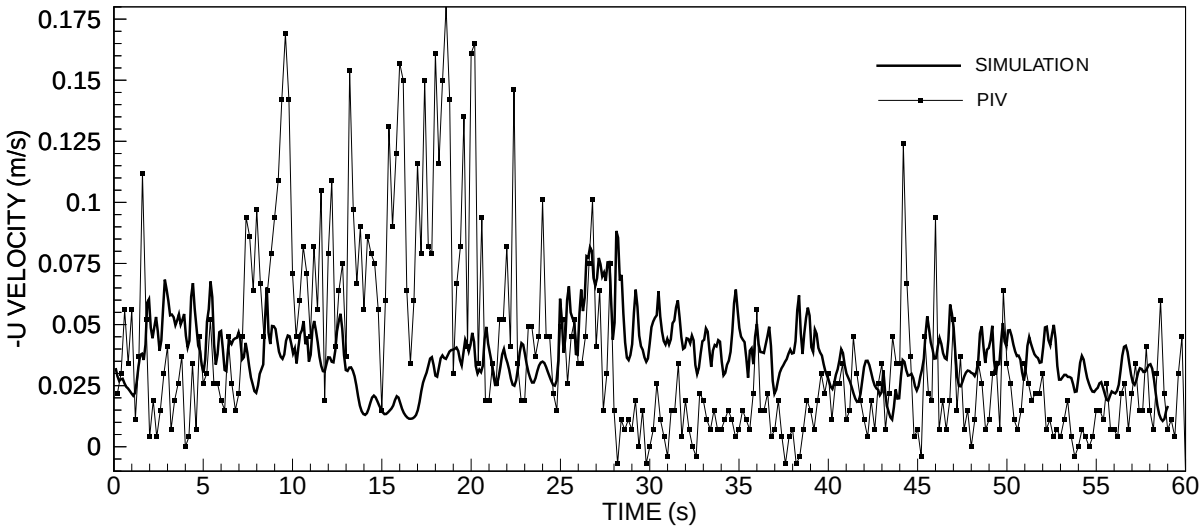

Fig. 7. Typical history of U velocity component in simulation and PIV (about 2 cm below water surface).

have either a stronger upward or downward component, depending on the radial location. Motion of the jet in and out of the plane results in this vertical component of flow to often occur in the plane of the PIV measurements. This results in a net instantaneous jet angle that is significantly different from 30^{o}. This results in the staircase pattern seen in Figure 9.

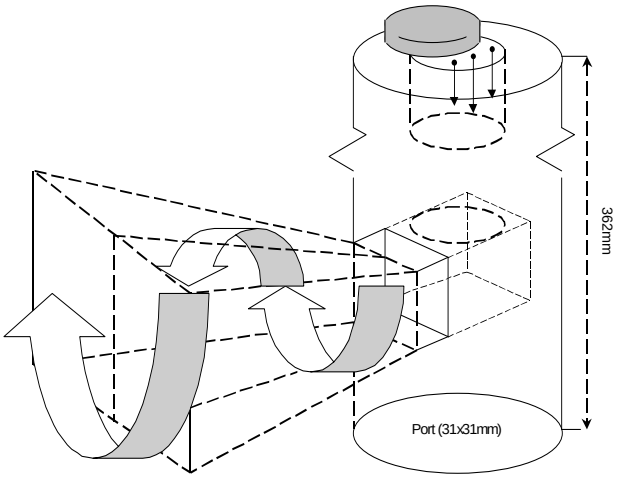

Fig. 8. Schematic of swirling flow in the PIV jet

As the jet moves in and out of the center plane at a given point, either the upward or downward moving portion of the spiral flow will be present. This causes the staircase shape to alternate. The time scale of this fluctuation, and corresponding in-out of plane motion is of the order of 0.2s. In addition, the entire jet chaotically alternates between shallow and deep penetration. The jet also has an in-out motion on a large time scale, resulting in the frequent intermittent disappearance of vectors close to the narrow face, for periods of about 7s. The simulation jet also has miniature staircase

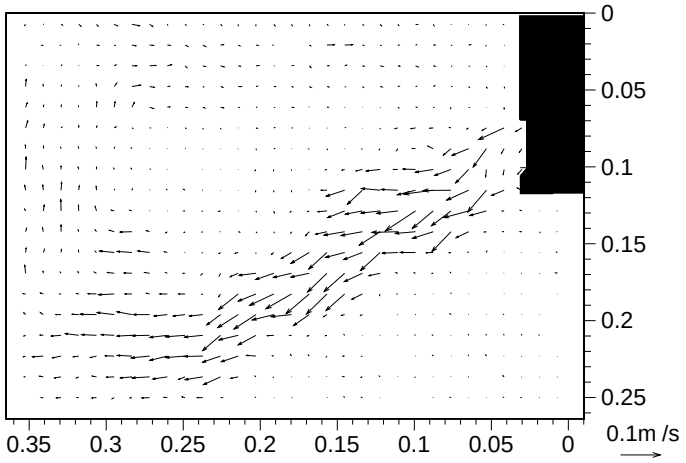

Fig. 9. Instantaneous PIV vector plot of the center plane.

patterns which result from jet wobble due solely to turbulence, which is consistent with previous work [14]. However the deviation from 30° is much smaller than the PIV measurement and the different staircases are out of phase.

This finding implies that the inlet swirl persists more than halfway across the mold. This may significantly affect the flow features in other regions of the mold and explain some of the discrepancies in the results. Thus it is necessary to incorporate the swirling inlet condition along with the in-out of plane motion in future simulations.

LES Simulation of Electromagnetic MFC Sensor

Figure 10 shows location of two MFC velocity sensors on half of the wideface of the mold. The sensors can be used to determine whether the flow pattern in the molten steel has only a single roll or a lower and upper (double) roll [5, 8]. The signals can also provide a measure of the strength of the velocities close to the top surface.

Each MFC sensor consists of two probes located close to each other behind the copper mold plates. Both probes emit a magnetic field. The flow of conducting steel through this magnetic field induces an electrical signal in each of the probes, according to Faraday's third law of electromagnetism. The time shift between prominent features of the two signals is a measure of the time taken by the flow to convect from one probe to the other. The average velocity in the region between the probes is then the distance between the probes divided by this time shift.

To enable comparisons of the MFC sensor signals with the numerical model, simulation results were extracted to predict the output of the probes. The horizontal velocity component convects the flow structures from one probe to the other. Prominent flow features appear in both signals, with a time shift corresponding to the average horizontal velocity between the probes. Thus, the horizontal velocity components calculated within the cells in the area beneath each probe head were first averaged in each plane parallel to the wideface. Next, the attenuation of the magnetic field strength with distance into the flow was taken into account by assuming that the induced signal strength decreased inversely with the square of the distance from the wideface, according to Figure 11. Thus, the overall simulated signal was calculated by taking a weighted average of the horizontal velocities calculated in the different planes beneath the probe head. Weighting factors were taken from Figure 11. The average of the two signals predicted at each probe indicates the best possible sensor output.

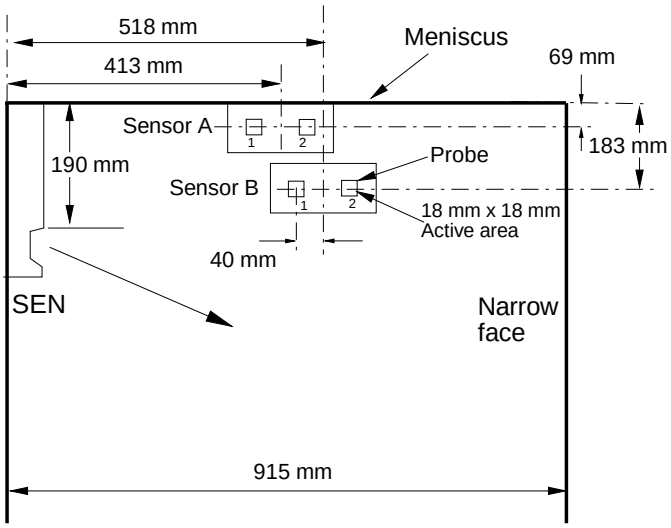

Fig. 10. MFC sensor location on water model

Figures 12 a) and (b) show typical simulated probe signals predicted for sensors A and B. The positions were scaled from Figure 10 dimensions to correspond with the 0.4 scale water model. At position A, near the liquid surface, the two probe signals are very similar, except for an obvious time shift. Thus, it is quite feasible that the average of the two signals could be extracted by the signal processing logic, without knowing the absolute velocities shown on the y axis. At position B, however, the two probe signals are very different. They are clearly not always the same basic signal offset in time, so it is likely that large errors might arise in predicting their average by the signal processing. The reason for this difference in

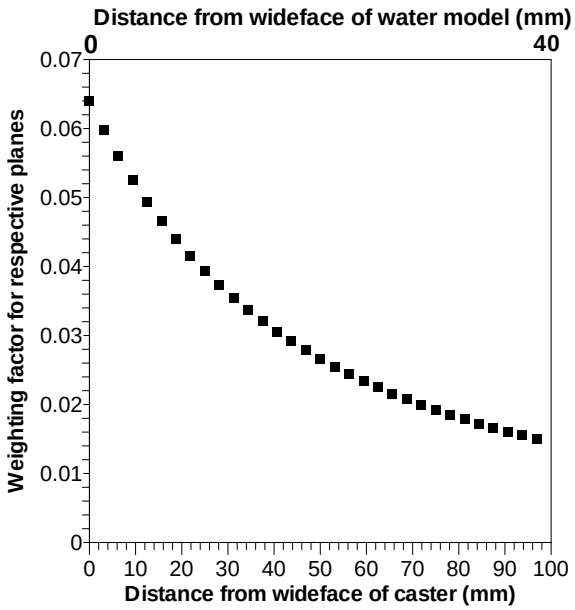

Fig. 11. Assumed weighting of velocities with distance from wideface by MFC probes

behavior of the signals at A and B can be understood by looking at the flow fields near the two sensors.

Figure 13 shows samples of instantaneous velocity-vector plots taken in two planes parallel to the wideface in the top region of the simulation. The upper roll at this instant is seen to consist of a set of distinct vortex structures, as opposed to the single large recirculation structure seen in the time average vector plot. The upper roll alternates chaotically between these two extremes.

Flow at position A near the top surface is seen to be relatively consistent, as velocities are mainly horizontal and similar at both probes. Comparing Figures 13a) and b) shows that variations through the mold thickness are less significant than the time variations, so the attenuation of the electromagnetic signal should not be important.

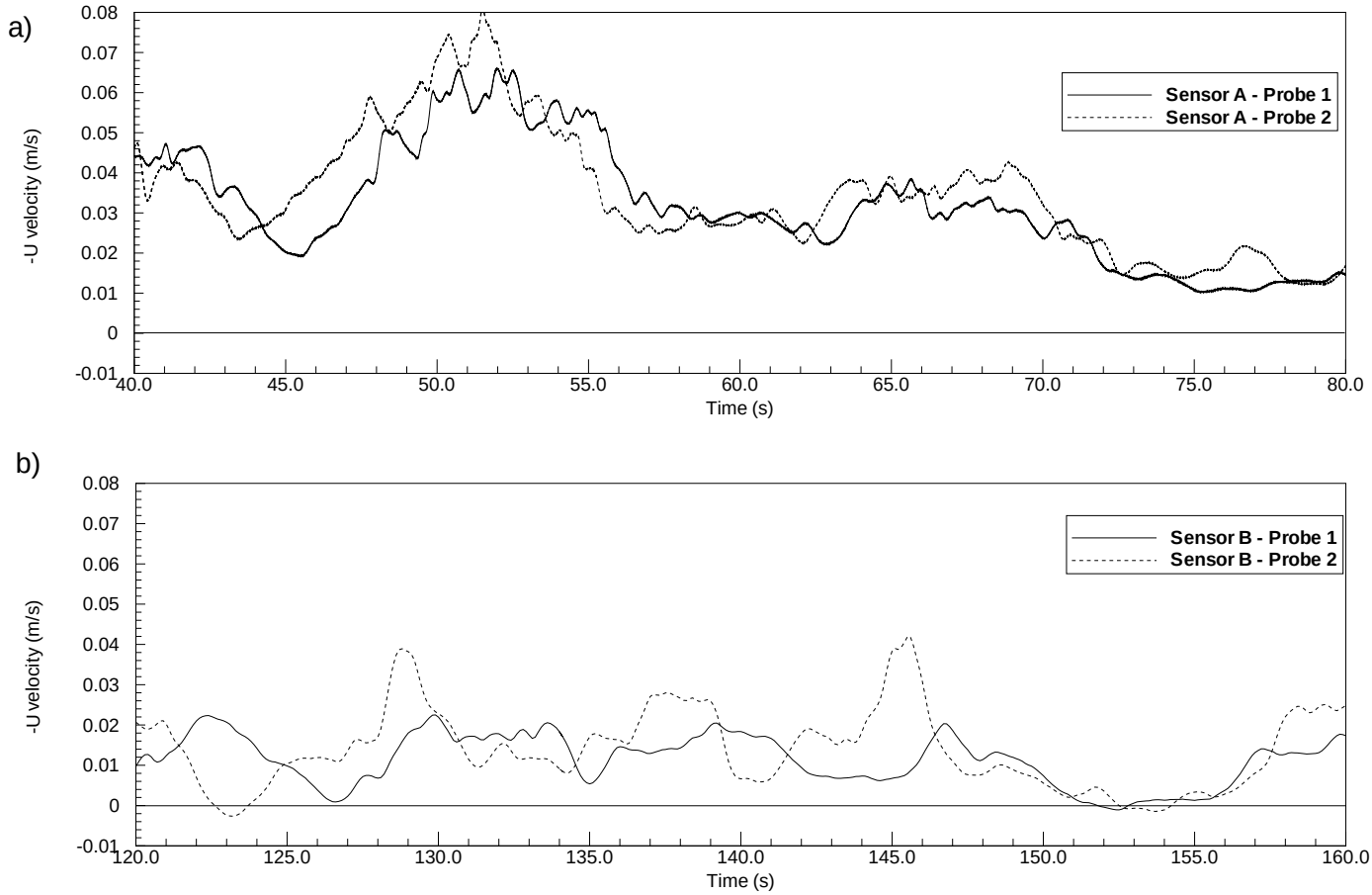

Fig. 12. Simulated Probe signals and MFC sensor output at locations A (a) and B (b).

Flow at position B is very different, however. The mean convection of vortices is not nearly horizontal. Flow past one probe often does not even reach the other probe. Thus, the probe signals may not always correlate (Figure 12 b). Figure 13 also shows how vortex structures traverse almost randomly across the caster, especially near the center of the roll. For Sensor A, the fluctuations appear to reverse the time shift for a few seconds (Figure 12 a) 70-72s). Velocities predicted at some probes indicate a real change in the direction of flow for several seconds (Sensor B Figure 12 b) 122-125s and 152-155s). Either of these situations might be falsely interpreted as a change between single and double roll patterns. In conclusion, this analysis suggests that the MFC sensor probes should be placed in regions of steady horizontal flow, such as found near the top surface.

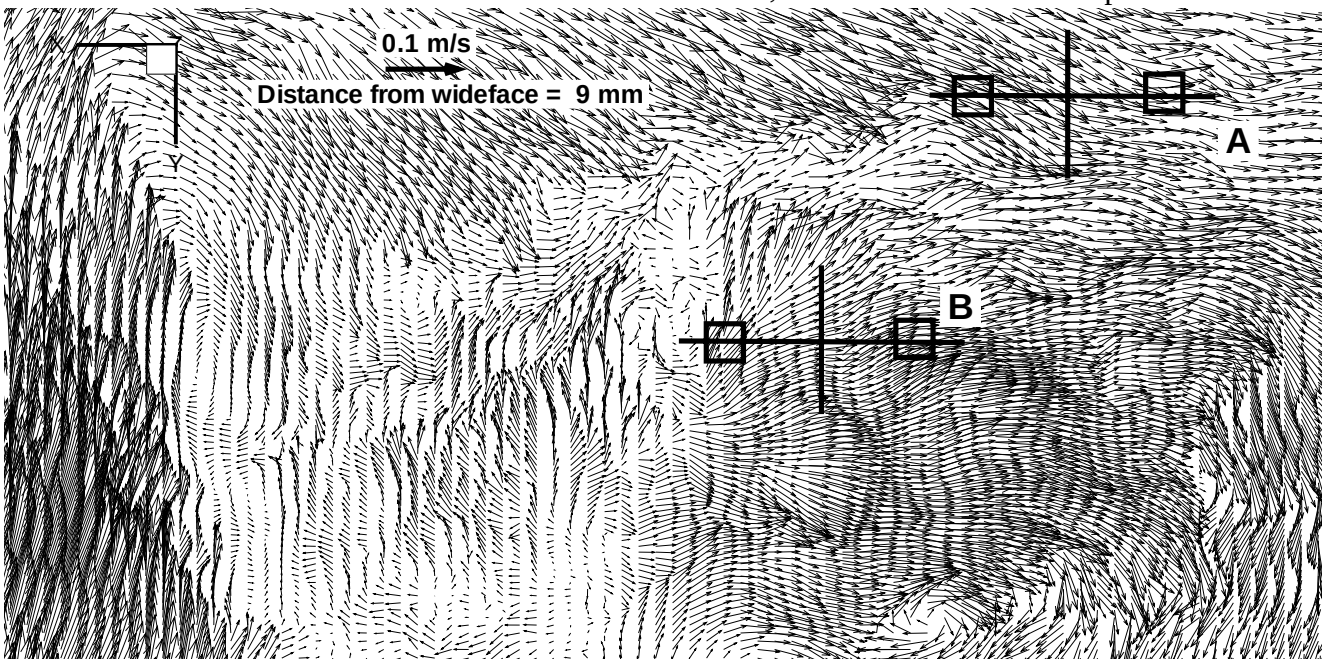

Fig. 13(a). Instantaneous simulated vector plot of the upper roll 9mm from wideface

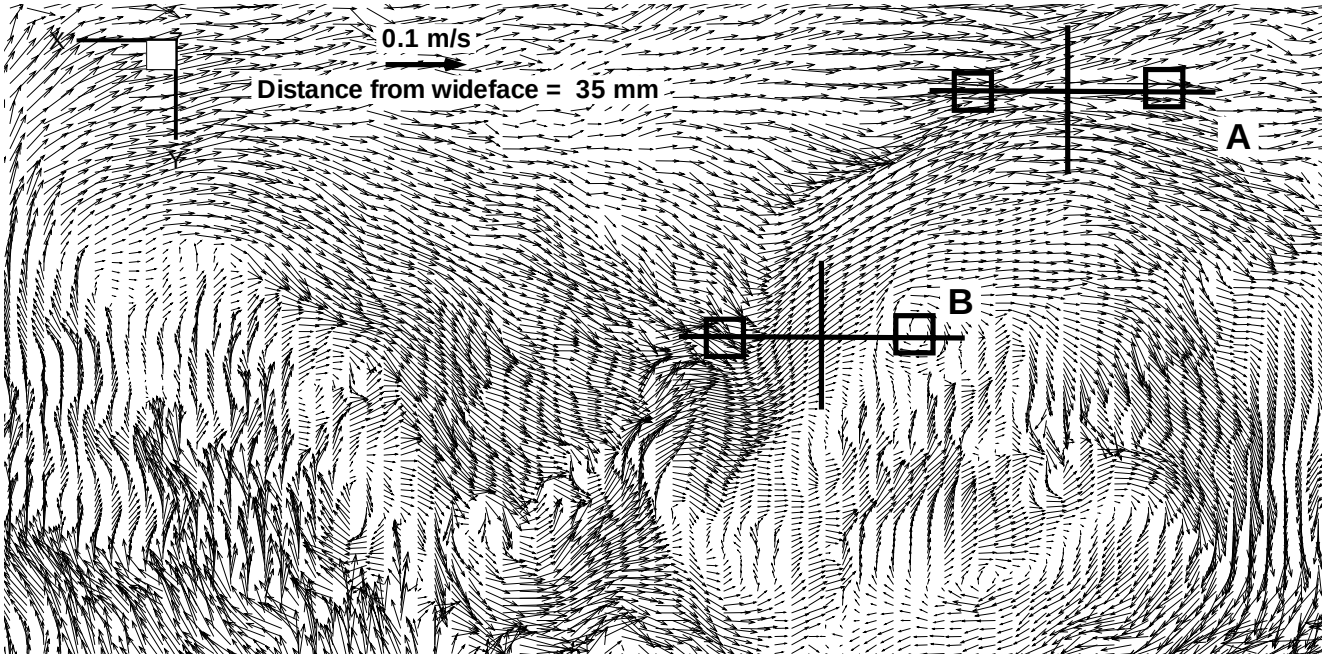

Fig. 13(b). Instantaneous simulated vector plot of the upper roll 35mm from wideface

Comparison of LES, K-ε, PIV, and MFC

Figure 14 a) shows an example of the screen output of the MFC sensor located on the caster at the LTV Steel plant. The gradually fluctuating shape of the signal is similar to the shape of the simulated probe signal in Figure 12 a). Figure 14 b) shows MFC output at A near the surface as a function of casting speed for Table I conditions. Each point is a 10s time average. The significant scatter has several potential causes, including variations in casting conditions between the 61 slabs in the plant trial.

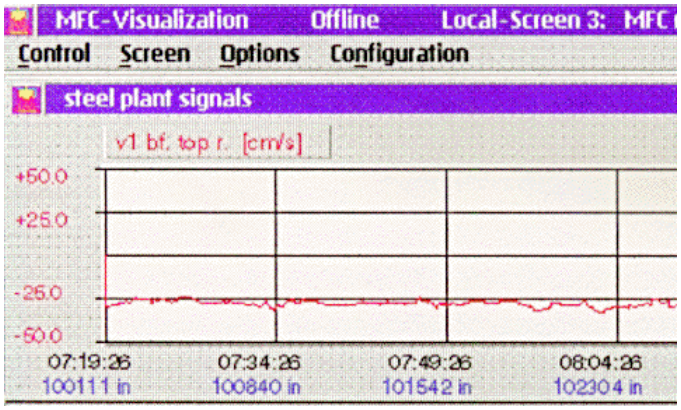

Fig. 14 a) MFC sensor output (1.8m wide slab; 0% argon, 1.25 m/min casting speed)

Qualitatively, all four of the flow analysis tools agree. The conditions under investigation always produce a classic double roll flow pattern, such as shown in Figure 6. Maximum velocities along the top surface are found midway between the SEN and narrow face, and fluctuations are great. Top surface velocities increase with casting speed.

The K-ε, LES, and PIV results are compared quantitatively in Figure 14 c) for flow along the top surface of the water model. The K-ε predictions agree very well with the PIV data. The LES predictions are low, perhaps due to differences in the inlet conditions assumed in the simulation. The LES sensor predictions are slightly lower than LES predictions along the top surface.

It is difficult to compare the MFC sensor data directly with the water model results due in part to the 0.4 scale factor. However, assuming Froude similarity means that the 0.63 m/min casting speed in the water model scales up by a factor of $\sqrt{1.0 / 0.4}$ to 1.0 m/min. in the caster. The average surface speed from the MFC sensor signal at 1.0 m/min is 0.20 m/s (Figure 14b). This agrees very well with the K-ε and PIV value of 0.19 m/s (scaled up from the maximum of 0.12 m/s in Figure 14c). This agreement is very encouraging, but further validation is needed to reconcile the LES model and to investigate conditions where argon gas is present.

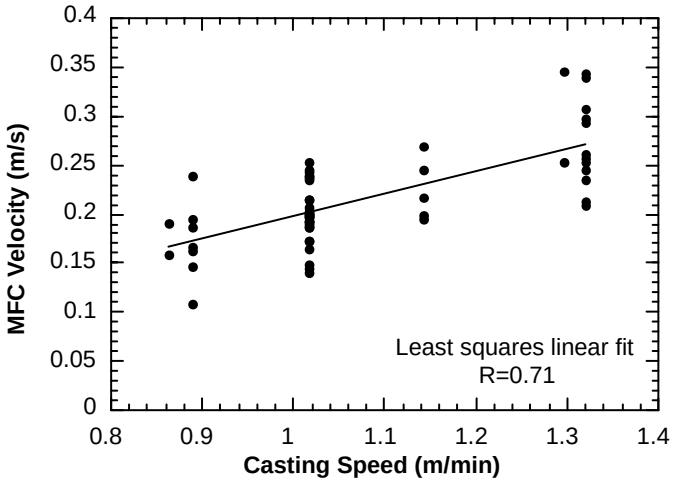

Fig. 14 b) MFC sensor output sorted by casting speed

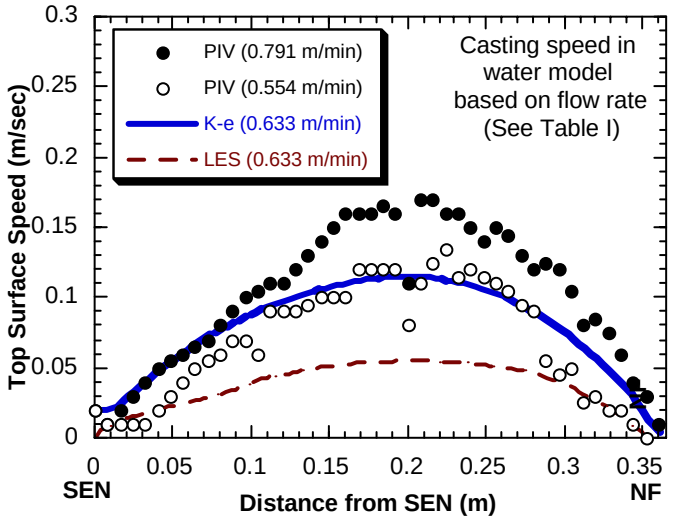

Fig. 14 c) Variation of time-average speed along top surface comparing PIV, K-ε, and LES

LES and PIV in the Lower Mold

Figure 15 is a 30-min time averaged vector plot of the velocities measured in the lower rolls of the water model. Considerable asymmetry can be seen between the left and right rolls, which persist even over this long time period.

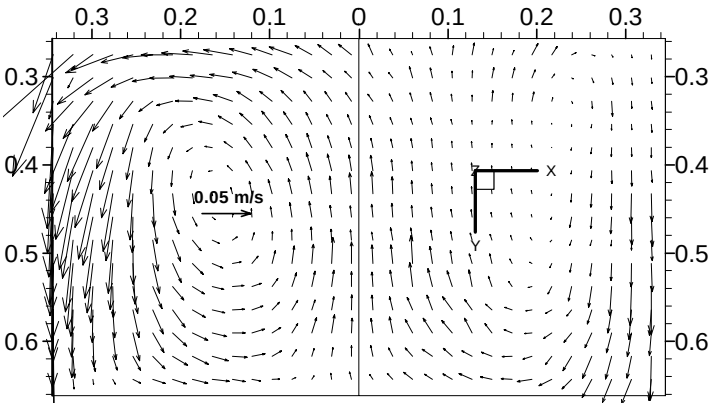

Fig. 15. Velocity vector in both of the lower rolls (30 min. time average).

There are two main features of this asymmetry that are especially significant. The first is the region of very low velocity below the impingement point on the right, which contrasts with the higher downward flow on the left. The second is the difference in the shapes and flow in the two lower rolls. The first was likely caused by an angular misalignment of the nozzle of the order of 1^{o} in the X-Z plane resulting in the jet on the right moving out of the center plane. Dye injection study for the same configuration, without change in the flow settings is consistent with this angular misalignment. The second is the upward moving flow below the SEN being directed towards the left. This suggests a period of time when the right roll is larger than the left. Study of the transient flow features over this 30-min. period reveals a repeating sequence of three features when: 1) Both rolls are about the same size for about 17s; 2) Right roll is larger than the left for about 30s and 3) A short-circuited structure forms and merges into the lower roll over about 10s, while both rolls are about the same size.

The simulation enforces symmetry by simulating only half of the domain with a symmetry boundary condition. The presence of this significant asymmetry necessitates the simulation of both halves of the water model / caster in future work. Figures 5 a) and (b) show an instant when the short circuit between the upward and downward flows of the lower roll has taken place and the downward motion of the location of the short circuit has begun.

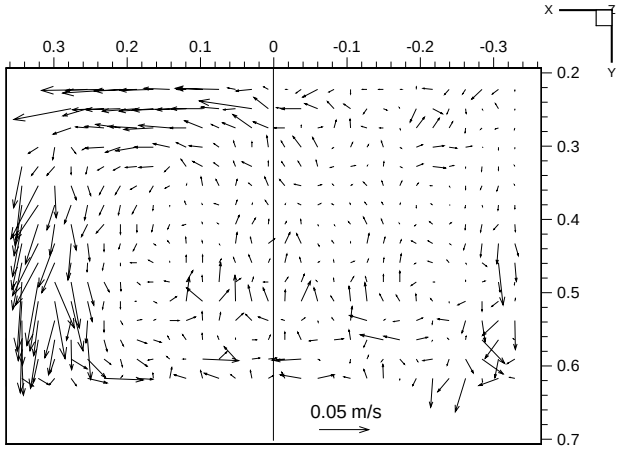

Fig. 16. Instantaneous PIV vector plot of lower rolls when both rolls are about the same size

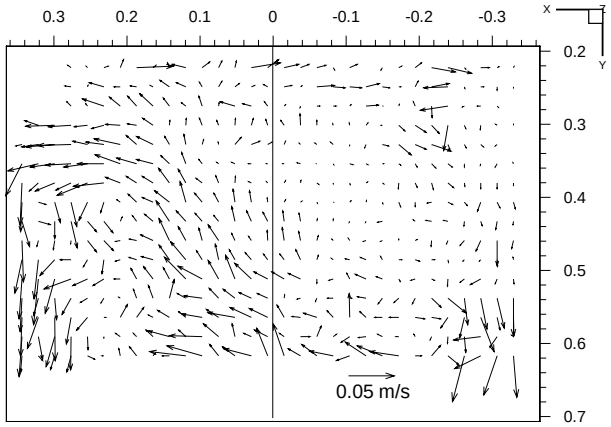

Fig 17. Instantaneous PIV vector plot of lower rolls when right roll is larger than the left

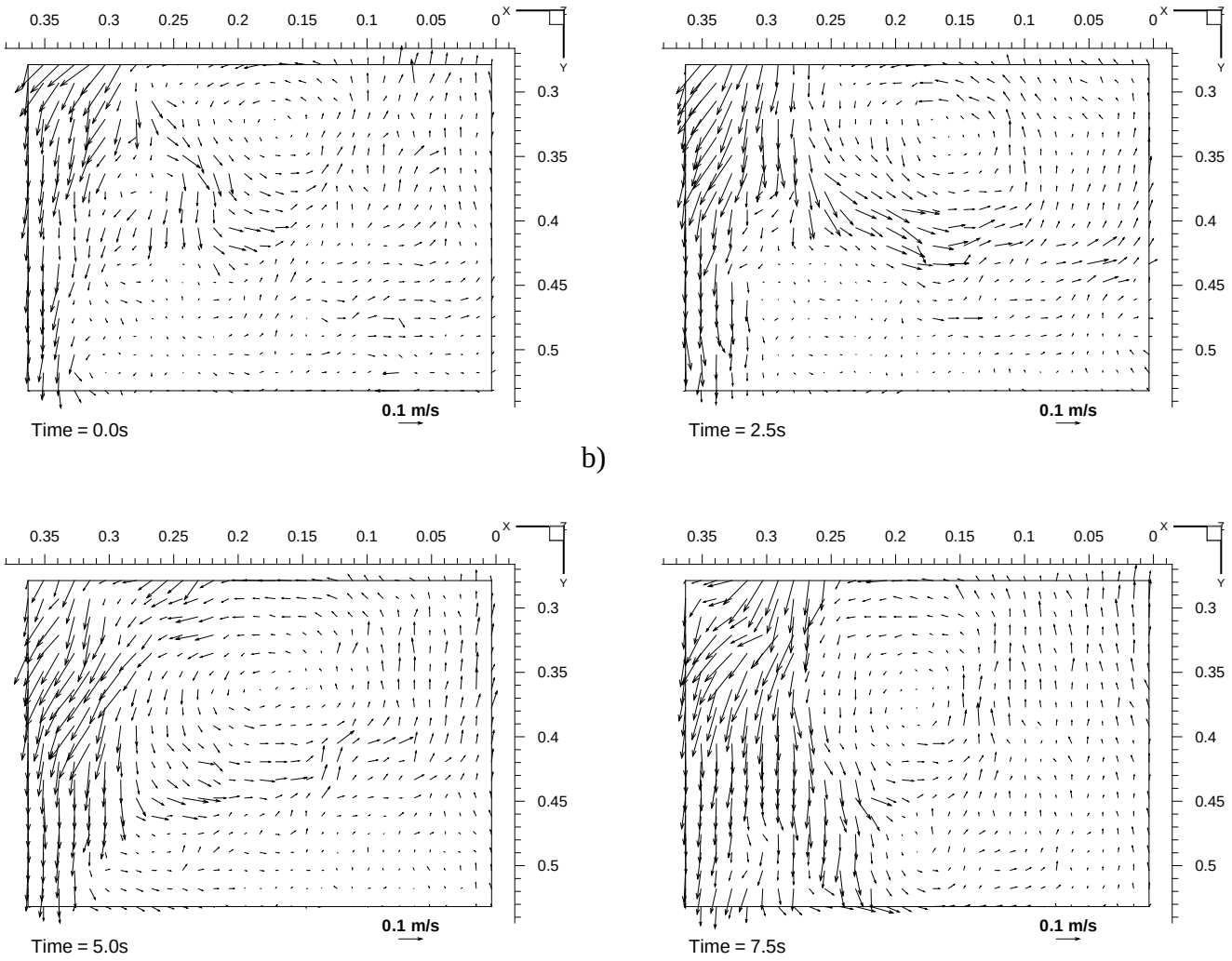

Fig. 18. Sequence of PIV images (a-d) showing formation and downward motion of the short-circuited structure over a time period of 7.5s

The transient sequence in the lower roll of both the simulation and PIV progresses as follows. Initially, both left and right rolls are about the same size, as shown in the instantaneous snapshot in Figure 16. This symmetrical configuration lasts for about 12s. This is followed by a period of around 17s when the right roll is larger than the left, as indicated in Figure 17 by the upward flow below the nozzle directed to the left. This in turn is followed by the sequence of instantaneous PIV vector plots shown in Figures 18 (a-d) which span 7.5s. Here the downward flow along the NF from the impingement point of the left jet turns sharply to the right, to form a short- circuited roll structure (a). This might be caused by pressure instabilities in the flow field. This structure then expands downward over a 7.5s period (b-d). This sequence repeats every 1 min.

Parts of this repeating sequence are seen in the simulation as well. Figure 19 shows an instant when the lower roll in the simulation is a single large recirculation region. Figure 20 shows a sequence identical to that in the PIV, where a short circuit structure is formed which expands downward. The time scale for this phenomenon is the same for PIV and simulation. This suggests that this short circuit structure is probably caused by turbulence and not by changes at the inlet or other disturbances which may be present in the PIV but not in the simulation.

This phenomenon is important when studying bubble or particle entrapment because it changes the transport phenomena in the lower roll.

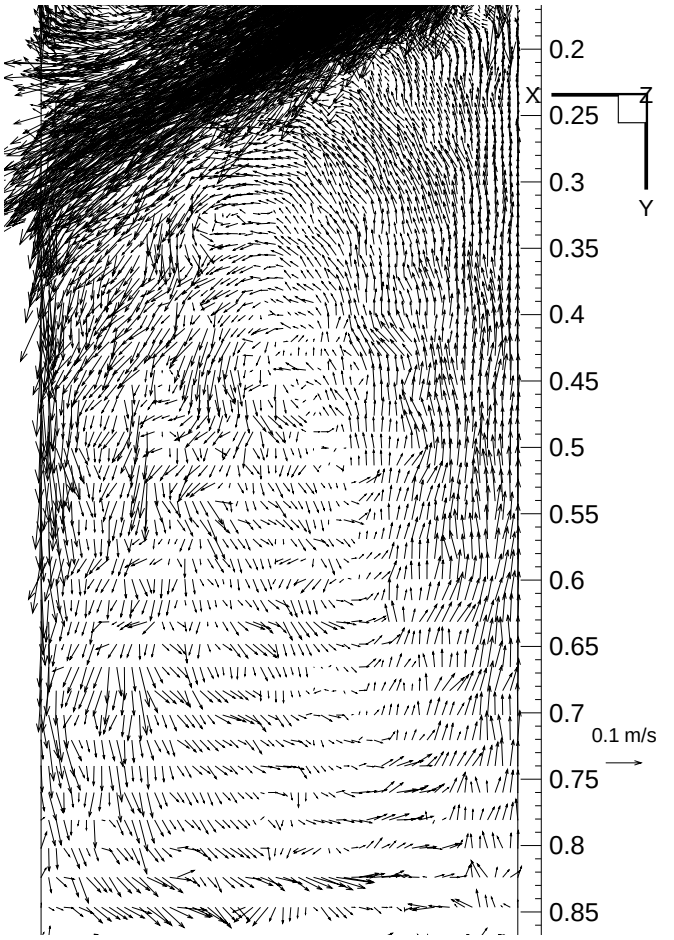

Fig. 19. Instantaneous simulation vector plot when lower roll is a large recirculation region

CONCLUSIONS

The turbulent flow of liquid steel in a continuous casting mold has been investigated with K-ε and LES computational models, water models, and plant measurements. Model predictions generally agree both qualitatively and quantitatively with velocities measured using PIV (Particle Image Velocimetry) on a 0.4-scale water model and with MFC sensors in a steel caster. The LES simulation slightly overpredicts velocity beneath the nozzle and under-predicts it along the top surface, likely due to oversimplified inlet conditions. Together, the numerical simulations, PIV and MFC results reveal deeper insight into flow in the continuous casting process, especially transient phenomena.

The inlet condition is very influential on flow in the mold. Strong swirl is generated at the port outlet by the 90^o oriented slide gate nozzle. This causes considerable in and out of plane motion, which persists at least halfway across the mold. This was not captured in the current LES simulation, which has a simple inclined fully-developed turbulent square duct flow as its inlet condition.

Flow across the top surface in the physical model varies by more than 100% of its mean value. This variation has a high frequency component (~1.5 Hz) which is also seen in the simulation. It also includes a low frequency component (time period of the order of 45s) with times of more than 5s when the horizontal velocities are 3-4 times larger than their mean values. This component is not seen in the simulation, so might be caused by fluctuations in the inlet conditions. This feature is likely significant to shear entrainment of liquid flux.

The LES simulation of the MFC sensor signals illustrates the great importance of locating the sensor in a stable region of the flow if accurate velocities are to be extracted. Sensors positioned in the current location near the top surface should accurately output both the direction and velocity history. The individual probes of sensors positioned deep in the recirculation zone experience very different transient flow fields, so cannot be relied upon to produce accurate velocities.

Although the entire geometry including the inlet nozzle and its port were symmetric, there was considerable, persistent, asymmetry between the two lower rolls. Flow in this region alternates through a sequence of flow phenomena, which repeats chaotically. One of the flow features involving short circuiting is seen in both the physical model and the simulation, suggesting that it is inherent to the turbulence and is not caused solely by the inlet conditions. This feature is important for particle motion and bubble entrapment, which are responsible for defects in the final product.

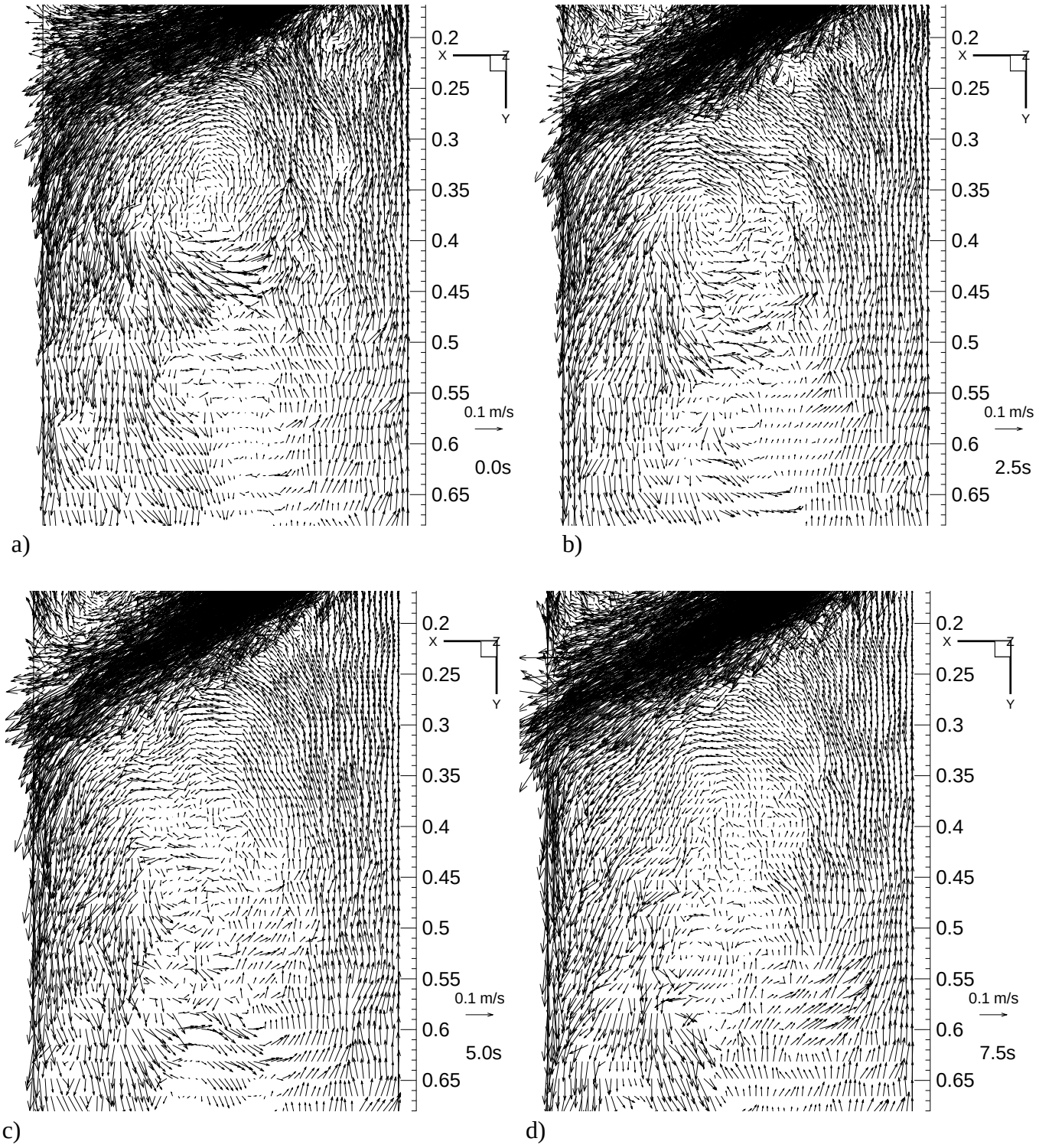

Fig. 20. Sequence of simulation images (a-d) showing formation and downward motion of the short-circuited structure over a time period of 7.5s

ACKNOWLEDGEMENTS

The authors would like to thank the National Science Foundation (NSF - Grant # DMI - 98-00274) and the Continuous Casting Consortium (CCC) at the University of Illinois at Urbana Champaign (UIUC) for their support of this research, the National Center for Supercomputing Applications (NCSA) at the UIUC for computing time, AEA technology for use of the CFX 4.2 program, and LTV Steel for use of the PIV system and access to PIV and MFC measurements.

REFERENCES

1. L.M. Mika, B.G. Thomas and F. Najjar: "Simulation of Fluid Flow Inside a Continuous Slab Casting Machine", *Metallurgical Transactions B*, 1990, vol. 21B, pp. 387-400.

2. D.E. Hershey, B.G. Thomas and F.M. Najjar: "Turbulent Flow through Bifurcated Nozzles", *International Journal for Numerical Methods in Fluids*, 1993, vol. 17, pp. 23-47.

3. F.M. Najjar, B.G. Thomas and D.E. Hershey: "Turbulent Flow Simulations in Bifurcated Nozzles: Effects of Design and Casting Operation", *Metallurgical Transactions B*, 1995, vol. 26B (4), pp. 749-765.

4. D. Xu, W.K. Jones and J.W. Evans: "PIV Physical Modeling of Fluid Flow in the Mold of Continuous Casting of Steel", in *Processing of Metals and Advanced Materials: Modeling, Deisgn and Properties*, B.Q. Li, eds., TMS, Warrendale, PA, San Antonio, TX, 1998, pp. 3-14.

5. M.B. Assar, P.H. Dauby and G.D. Lawson: "Opening the Black Box: PIV and MFC Measurements in a Continuous Caster Mold", in *Steelmaking Conference Proceedings*, vol. 83, ISS, Warrendale, PA, 2000,

6. M. Gharib and C.E. Willart: "Digital Particle Image Velocimetry", *Experiments in Fluids*, 1991, vol. 10, pp. 181-193.

7. Dantec Flow Technology: *User's Guide, V. 2.01*, 777 Corporate Drive, Mahwah, New Jersey 07430, 1998.

8. K.U. Kohler, P. Andrzejewski, E. Julius and H. Haubrich: "Steel Flow Velocity Measurement and Flow Pattern Monitoring in the Mould", in *Steelmaking Conference Proceedings*, vol. 78, ISS, Warrendale, PA, 1995, pp. 445-449.

9. J. Tannehill, D. Anderson and R. Pletcher: *Computational Fluid Dynamics and Heat Transfer*, Taylor and Francis, Washington, DC, 1997.

10. R. Madabushi and S.P. Vanka: "Large Eddy Simulation of Turbulence-Driven Secondary Flow in a Square Duct", *Physics of Fluids*, 1991, vol. 3 (11), pp. 2734-2475, Nov. issue.

11. AEA Technology: *CFX 4.2 Users Manual*, 1700 N. Highland Rd., Suite 400, Pittsburgh, PA 15241, 1998.

12. H. Bai and B.G. Thomas: "Two-phase flow in tundish nozzles during continuous casting of steel slabs", *Materials Processing in the Computer Age III*, V. Voller and H. Henein, eds., Nashville, TN, TMS, Warrendale, PA, March 12-16, 2000.

13. B.G. Thomas: *Mathematical Models of Continuous Casting of Steel Slabs*, Continuous Casting Consortium, University of Illinois at Urbana-Champaign, Report, 1998.

14. R.V. Wilson and A.O. Demuren: "Numerical simulation of turbulent jets with rectangular cross section", *ASME J of Fluids Eng*, 1998, vol. 120 (Jun), pp. 285-290.

For further information on this paper, please contact Brian G. Thomas at 1206 West Green Street, Urbana, IL, 60801; Ph: 217-333-6919; Fax: 217-244-6534; email: bgthomas@uiuc.edu